

Cite this: *J. Mater. Chem. C*, 2021, 9, 7392

# Study of configuration differentia and highly efficient deep-red thermally activated delayed fluorescent organic light-emitting diodes based on phenanthro[4,5-*fg*h]quinoxaline derivatives†

Anqi Shang,<sup>‡</sup> Tong Lu,<sup>‡</sup> Hui Liu,<sup>a</sup> Chunya Du,<sup>a</sup> Futong Liu,<sup>a</sup> Dongyan Jiang,<sup>a</sup> Jiarui Min,<sup>b</sup> Haiquan Zhang\*<sup>b</sup> and Ping Lu<sup>id</sup>\*<sup>a</sup>

The development of efficient thermally activated delayed fluorescent (TADF) materials with a deep-red emission (emission wavelength beyond 620 nm) remains a great challenge in the field of organic light-emitting diodes (OLEDs). In this work, a series of structural isomers are successfully obtained by attaching an electron-donor triphenylamine (TPA) group to the various positions of two types of planar acceptor units, PQP and PQC. Interestingly, the *trans*-PyCNTPA and *trans*-PyPTPA all exhibit much higher photoluminescence quantum yields ( $\Phi_{\text{PL}}$ ) (87% and 81%) than their respective *cis*-isomers, *cis*-PyCNTPA (19%) and *cis*-PyPTPA (12%). The theoretical calculations and dynamic studies indicate the effective suppression of the nonradiative decay processes in *trans*-isomers. The *trans*-PyCNTPA and *cis*-PyCNTPA show relatively small  $\Delta E_{\text{ST}}$  and efficient reverse intersystem crossing to ensure the complete utilization of triplet excitons, indicating that the TADF characteristics are regulated by the co-acceptor of the CN unit owing to its strong electron-withdrawing property. As a result, a deep-red TADF-OLED based on *trans*-PyCNTPA is achieved with a maximum external quantum efficiency (EQE) of 15.5% at 668 nm, CIE coordinates of (0.66, 0.35) and stable electroluminescence spectra at different voltages. The results present an efficient method to develop efficient red TADF emitters by isomer optimization strategy.

Received 4th April 2021,  
Accepted 15th May 2021

DOI: 10.1039/d1tc01562a

rsc.li/materials-c

## Introduction

Materials with emission wavelength in a deep-red/near infrared (NIR) region are of particular importance owing to their wide applications in bioimaging,<sup>1–5</sup> chemosensing,<sup>6–8</sup> night-vision-devices,<sup>9,10</sup> information-secured displays,<sup>11–13</sup> and organic light-emitting diodes (OLEDs),<sup>14–24</sup> etc. So far, the deep-red/NIR fluorescent materials with good performance in OLEDs still remain rare. The high photoluminescence quantum yield ( $\Phi_{\text{PL}}$ ) and exciton utilization efficiency ( $\Phi_{\text{EUE}}$ ) need to be fulfilled simultaneously to acquire satisfactory external quantum efficiency (EQE) in OLEDs according to the spin statistics theory.<sup>25</sup> In this case, the thermally activated delayed fluorescence (TADF) emitter becomes the recent concern mainly because of the promising full exciton utilization through the efficient reverse intersystem crossing (RISC) process.<sup>26–30</sup> The very small singlet–triplet

energy gap ( $\Delta E_{\text{ST}}$ ) is the basic parameter to achieve effective TADF effect through RISC.  $\Delta E_{\text{ST}}$ , which directly restricts the magnitude of the intersystem crossover rate, is expressed as follows:<sup>31,32</sup>

$$\Delta E_{\text{ST}} = 2J = 2\phi_{\text{h}}\phi_{\text{c}} \left| \frac{1}{r_{\text{h-c}}} \right| \phi_2\phi_1 \quad (1)$$

where  $J$  represents the singlet–triplet electron exchange energy, and  $|r_{\text{h-c}}|$  is the distance between the positive charge center and the negative charge center. Therefore, the small  $\Delta E_{\text{ST}}$  can be realized by creating a twisted donor–acceptor (D–A) molecular structure with sufficient separation between the highest occupied molecular orbital (HOMO) and the lowest unoccupied molecular orbital (LUMO).<sup>33,34</sup>

Generally,  $\Phi_{\text{PL}}$  is determined by the following equations:<sup>35</sup>

$$\Phi_{\text{PL}} = \frac{K_{\text{r}}}{K_{\text{r}} + K_{\text{nr}}} \quad (2)$$

$$K_{\text{nr}} \propto \alpha e^{-\beta\Delta E} \quad (3)$$

where  $K_{\text{r}}$  is the rate constant of radiative decay,  $K_{\text{nr}}$  is the nonradiative decay rate constant,  $\alpha$  and  $\beta$  are proportionality constants, and  $\Delta E$  is the energy gap between the zero-vibrational

<sup>a</sup> State Key Laboratory of Supramolecular Structure and Materials, Jilin University, Qianjin Street No. 2699, Changchun, 130012, P. R. China. E-mail: lup@jlu.edu.cn

<sup>b</sup> State Key Laboratory of Metastable Materials Science and Technology, Yanshan University, Hebei Street No. 438, Qinhuangdao, 066004, P. R. China. E-mail: cnhqzhang@ysu.edu.cn

† Electronic supplementary information (ESI) available. See DOI: 10.1039/d1tc01562a

‡ Dr Anqi Shang and Dr Tong Lu contributed equally to this work.

levels of  $S_1$  and the higher-vibrational levels of  $S_0$  states. Therefore, with the reduction of  $\Delta E$  in the deep-red/NIR zone, the vibrational overlap between  $S_0$  and  $S_1$  will manifest an exponential increase of substantial energy loss *via* non-radiative processes, leading to a relatively low  $\Phi_{PL}$ .<sup>36,37</sup> According to the Franck–Condon transition principle and Fermi's golden rule, small orbital overlaps in TADF materials will inevitably result in small transition dipole moments ( $M$ ) and thus lead to a small oscillator strength ( $f$ ) between the  $S_1$  and  $S_0$  states, which is not conducive to obtain a high  $\Phi_{PL}$ .<sup>38</sup> Consequently, it is still a formidable challenge to achieve highly efficient deep-red/NIR fluorescent materials and OLEDs with high  $\Phi_{PL}$  and  $\Phi_{EUE}$ .<sup>39–47</sup>

Pyrene is an interesting representative of polyaromatic hydrocarbons (PAH) with a very simple structure of four fused benzene rings. Combination of rigidity and planarity in molecular structure entitles pyrene with favorable  $\pi$ -electron flow, high  $\Phi_{PL}$  and controllable excimer formation, *etc.*<sup>48</sup> Functionality of the pyrene skeleton to improve its electronic properties has been a hot topic in an optoelectronic field in the past years, especially for the application in OLEDs.<sup>49–53</sup> In prior studies, N-atom containing heterocyclic compounds are commonly utilized in OLEDs because the  $sp^2$  or  $sp^3$  hybridization features of N-atoms are beneficial to enhancing the electron and hole injection ability in OLEDs.<sup>54</sup> In this case, the oxidation of pyrene and further treatment with *o*-phenylenediamine derivatives could facilely afford the corresponding N-heterocyclic phenanthro[4,5-*fg*h]quinoxaline units, which possess planar molecular structures to efficiently reduce the vibrational and rotational channels, suppress the non-radiative transitions to some extent and obtain relatively high  $\Phi_{PL}$ . In addition, such phenanthro[4,5-*fg*h]quinoxaline units could be expected to have relatively low LUMO energy levels and favor the application in deep-red/NIR light-emitting materials as the suitable electron-acceptors. The 1, 3, 6, 8 positions of pyrene are easily accessible, which provides multiple ways to modify the molecular structures and fine-tune the materials' functions.<sup>55</sup> When the phenanthro[4,5-*fg*h]quinoxaline unit is formed, the substitutions at 1 (6) and 3 (8) positions in various ways can generate structural isomers conveniently.<sup>56,57</sup> The isomeric strategy may present a promising method to investigate the influence of structure–property relationship, comparatively analyze the isomeric effect and extend the structural diversity of high-efficiency TADF emitters. The isomeric strategy may present a promising method to investigate the influence of structure–property relationship, comparatively analyze the isomeric effect and extend the structural diversity of high-efficiency TADF emitters.

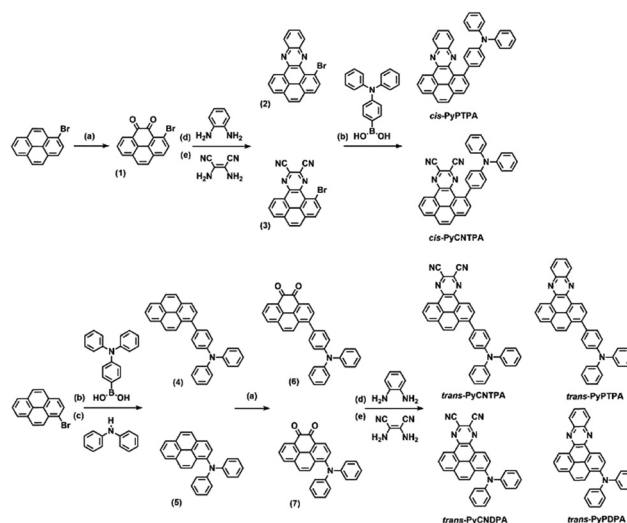
The isomeric strategy may present a promising method to investigate the influence of structure–property relationship, comparatively analyze the isomeric effect and extend the structural diversity of high-efficiency TADF emitters. Based on these consideration, in this work, four positional isomers, *cis*-PycNTPA, *cis*-PyPTPA, *trans*-PycNTPA and *trans*-PyPTPA, are developed in which the bulky triphenylamine (TPA) is employed as the donor owing to its excellent electron-donating capability, and electron-accepting phenanthro[4,5-*fg*h]quinoxaline-10,11-benzene (PQP) and phenanthro[4,5-*fg*h]quinoxaline-10,11-dicarbonitrile (PQCN) are adopted as the acceptor. PQCN is designed by introducing two CN groups

into the PQP unit as the co-acceptor to increase the electron-withdrawing strength and red-shift the emission spectra, which might contribute to obtain a small  $\Delta E_{ST}$  and promote the RISC process according to the formulas 2 and 3. In addition, *trans*-PycNDPA and *trans*-PyPDPA using diphenylamine (DPA) as the donor are also synthesized as the model compounds to investigate the function of an extra benzene ring in *trans*-PycNTPA and *trans*-PyPTPA. All the six compounds show twisted patterns caused by the relatively big steric hindrance of TPA and DPA, which diminish aggregation caused quenching (ACQ) effect to some extent. The introduction of bridging benzene in *trans*-PycNTPA and *trans*-PyPTPA could balance the relationship between the small  $\Delta E_{ST}$  and high  $\Phi_{PL}$  for red light-emitting materials. The positional change is found to significantly affect the photophysical properties and the *trans*-isomers all exhibit nearly 4-folded higher  $\Phi_{PL}$ s as compared with their *cis*-counterparts. The *trans*-PycNTPA, *trans*-PycNDPA and *cis*-PycNTPA show obvious TADF features suggesting that the introduction of the CN group is crucial to obtain a small  $\Delta E_{ST}$  to realize the RISC process. As a result, *trans*-PycNTPA exhibits a small  $\Delta E_{ST}$  of 0.11 eV and a high  $\Phi_{PL}$  of 87% in the doped film. The doped OLED based on *trans*-PycNTPA is achieved with an EQE of 15.5% and a deep-red emission peaking at 668 nm. These results reveal that the fine modulation of molecular structures and rational *cis*-/*trans*-isomeric effects all are relative to their performance, which is very important for the design of high-efficiency deep-red/NIR TADF materials.

## Results and discussion

### Synthesis and characterization

The synthetic routes of *cis*-PycNTPA, *cis*-PyPTPA, *trans*-PycNTPA, *trans*-PyPTPA, *trans*-PycNDPA and *trans*-PyPDPA are illustrated in Scheme 1. The starting material 1-bromine pyrene was obtained



**Scheme 1** Synthetic routes and molecular structures of *cis*-PyPTPA, *cis*-PycNTPA, *trans*-PycNTPA, *trans*-PyPTPA, *trans*-PycNDPA and *trans*-PyPDPA. (a)  $\text{CH}_2\text{Cl}_2$ , ACN,  $\text{H}_2\text{O}$ ,  $\text{NaIO}_4$ ,  $\text{RuCl}_3$ ; (b) Tol/ $\text{H}_2\text{O}$ ,  $\text{K}_2\text{CO}_3$ ,  $\text{Pd}(\text{PPh}_3)_4$ ,  $90^\circ\text{C}$ ; (c) Tol,  $\text{Pd}_2(\text{dba})_3$ ,  $t\text{-BuOK}$ ,  $(t\text{-Bu})_3\text{PhBF}_4$ ,  $110^\circ\text{C}$ ; (d) AcOH,  $125^\circ\text{C}$ . (e) AcOH,  $125^\circ\text{C}$ .

via a commercial source. The intermediate 1-bromine-pyrene-2,3-dione (1) was synthesized by one step oxidation of 1-bromine pyrene using sodium periodate as an oxidant in the presence of the  $\text{RuCl}_3$  catalyst. 1-Bromine-phenanthro[4,5-*fg*h]quinoxaline-10,11-benzene (2) and 1-bromine-phenanthro[4,5-*fg*h]quinoxaline-10,11-dicarbonitrile (3) were achieved by the similar cyclization reactions between 1 with *o*-phenylenediamine and diaminomaleonitrile, respectively. And then, the target compounds *cis*-PyPTPA and *cis*-PyCNTPA were produced through the Suzuki cross-coupling reaction between (4-(diphenylamino) phenyl) boronic acid and (2) and (3), respectively. For the synthesis of the other four compounds with *trans*-configuration, the different synthesis routes were adopted. The intermediate *N,N*-diphenyl-4-(1-pyrenyl) benzenamine (4) was synthesized through Suzuki cross-coupling reactions between 1-bromine pyrene and (4-(diphenylamino) phenyl) boronic acid, and *N,N*-diphenyl-1-pyrenamine (5) was achieved through the Buchwald-Hartwig cross-coupling reaction between 1-bromine pyrene and diphenylamine. And then, 4 and 5 were both oxidized to get *trans*-isomer 9-triphenylamine-pyrene-2,3-dione (6) and 9-diphenylamine-pyrene-2,3-dione (7) with the catalyst of  $\text{RuCl}_3$ . Finally, the target products were all conveniently afforded by cyclization reactions with good yields. *trans*-PyCNTPA and *trans*-PyCNDPA were synthesized by the cyclization reaction of the diaminomaleonitrile with intermediates 6 and 7, respectively. For the synthesis of *trans*-PyPTPA and *trans*-PyPDPA, the similar procedure was followed but using *o*-phenylenediamine as the reactant instead of diaminomaleonitrile. The purity and chemical structures of the six target molecules were characterized by NMR, mass spectroscopy and elemental analysis. The details of the synthesis process are all summarized in the ESI†

### Theoretical calculations

To further explore the geometrical and structure–property relationship of these isomers, density functional theory (DFT) and time-dependent DFT calculations were performed using the Gaussian 09 package at the level of B3LYP/6-31G(d,p). Fig. 1 displays the optimization of ground state configurations and the frontier molecular orbital (FMO) distributions. By virtue of the large steric resistance between TPA/DPA donors and planar PQP and PQCN acceptors in the optimized geometries, a highly distorted dihedral angle of  $58.2^\circ$  for *cis*-PyCNTPA,  $69.5^\circ$  for *cis*-PyPTPA,  $53.8^\circ$  for *trans*-PyCNTPA,  $60.1^\circ$  for *trans*-PyCNDPA,  $54.7^\circ$  for *trans*-PyPTPA and  $64.5^\circ$  for *trans*-PyPDPA were observed, which was helpful for the efficient separation of FMOs and suppression of intermolecular interactions. Compared with the stretching structure molecule of *trans*-PyCNTPA and *trans*-PyPTPA, *cis*-PyCNTPA and *cis*-PyPTPA all possessed more distorted structure and bigger twisted torsion angles between the donor and acceptor, which led to fully separated FMOs. The HOMOs were dominantly located on the TPA segments owing to the good electron-donating property in *trans*-PyCNTPA and *trans*-PyPTPA with a little distribution on pyrene. When the donor was changed from TPA to DPA in *trans*-PyCNDPA and *trans*-PyPDPA, the HOMOs were mainly located on the DPA units with sizable distributions on the pyrene group, which indicated that reducing a benzene ring would

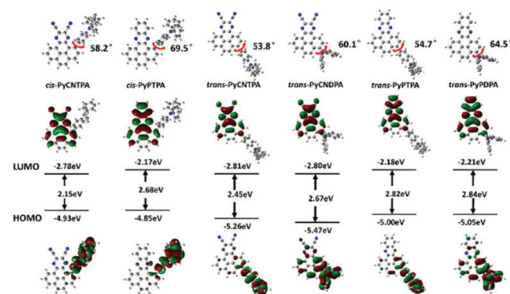


Fig. 1 Optimized ground-state ( $S_0$ ) geometries, HOMO and LUMO distributions of *cis*-PyCNTPA, *cis*-PyPTPA, *trans*-PyCNTPA, *trans*-PyCNDPA, *trans*-PyPTPA and *trans*-PyPDPA.

Table 1 Summary of physical properties of *cis*-PyCNTPA, *cis*-PyPTPA, *trans*-PyCNTPA, *trans*-PyCNDPA, *trans*-PyPTPA and *trans*-PyPDPA

Compound	$T_d$ ( $^\circ\text{C}$ )	$\lambda_{\text{max,abs}}^a$ (nm) sol	$\lambda_{\text{max,PL}}^b$ (nm) sol/neat film	HOMO/ LUMO <sup>c</sup> (eV)	$\Delta E_g^d$ (eV)
<i>cis</i> -PyCNTPA	427	285,347,440	607/685	−5.23/−3.56	0.10
<i>cis</i> -PyPTPA	418	287,351,453	517/565	−5.31/−3.38	0.34
<i>trans</i> -PyCNTPA	436	285,364,467	602/690	−5.25/−3.60	0.11
<i>trans</i> -PyPTPA	435	288,349,446	514/560	−5.33/−3.39	0.34
<i>trans</i> -PyCNDPA	397	282,365,463	615/715	−5.35/−3.60	0.08
<i>trans</i> -PyPDPA	401	293,354,461	536/590	−5.37/−3.38	0.29

<sup>a</sup>  $\lambda_{\text{max,abs}}$ : absorption maximum in toluene. <sup>b</sup>  $\lambda_{\text{max,PL}}$ : emission peak in toluene and neat thin films. <sup>c</sup> HOMO/LUMO energy levels measured by cyclic voltammetry measurement. <sup>d</sup>  $\Delta E_g$ : calculated from HOMO and LUMO.

induce a small overlap of HOMO and LUMO energy level. The LUMOs were mainly located on the acceptors of PQP and PQCN segments. For *cis*-PyCNTPA, *trans*-PyCNTPA and *trans*-PyCNDPA in which the CN was chosen as the co-acceptor, their LUMOs all lied about 0.60 eV lower than those of *cis*-PyPTPA, *trans*-PyPTPA and *trans*-PyPDPA, respectively. This could be attributed to the stronger electron-withdrawing ability of PQCN compared to PQP which might lead to a red-shifted emission. To further explore the  $S_1$  and  $T_1$  states, natural transition orbital (NTO) analysis was also studied by using time-dependent density functional theory (TD-DFT) calculation (Fig. S7, ESI†). The *cis*-PyCNTPA, *trans*-PyCNTPA and *trans*-PyCNDPA all possessed relatively smaller  $\Delta E_{\text{ST}}$  than *cis*-PyPTPA, *trans*-PyPTPA and *trans*-PyPDPA, which might produce more effective RISC processes from  $T_1$  to  $S_1$ . The *trans*-isomers all allowed radiative transitions from the  $S_1$  to  $S_0$ , which could be confirmed by the comparatively higher oscillator strengths of the  $S_1 \rightarrow S_0$  transitions than *cis*-isomers, meaning that higher PL efficiencies could be expected in *trans*-isomers. Their calculated  $\Delta E_g$ , HOMO and LUMO energy levels, and  $\Delta E_{\text{ST}}$  values are all summarized in Table 1 and Table S1 (ESI†).

### Thermal and electrochemical properties

In order to determine the thermal stability of these six compounds, thermal gravimetric analysis (TGA) and the differential scanning calorimetry (DSC) were used to test the thermal performance in a nitrogen atmosphere and the results are shown in Fig. 2a and Fig. S8 (ESI†). During the whole measurements, these six compounds all displayed good thermal stabilities and the

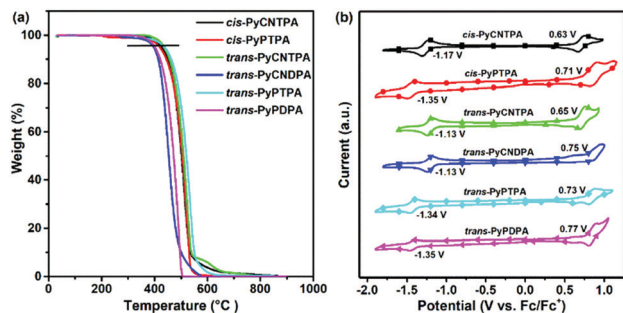


Fig. 2 TGA traces recorded at a heating rate of  $10\text{ }^{\circ}\text{C min}^{-1}$  (a) and cyclic voltammograms (b) of *cis*-PyCNTPA, *cis*-PyPTPA, *trans*-PyCNTPA, *trans*-PyCNDPA, *trans*-PyPTPA and *trans*-PyPDPA.

decomposition temperatures ( $T_d$ , corresponding to 5% weight loss) were found in the range of  $399\text{ }^{\circ}\text{C}$  to  $442\text{ }^{\circ}\text{C}$ . The six compounds having good thermal stability, during the whole measurement, exhibited high glass transition temperatures in the range of  $106\text{ }^{\circ}\text{C}$  to  $125\text{ }^{\circ}\text{C}$ . This ensured the possibility to obtain uniform and amorphous films upon thermal evaporation, which was conducive to device fabrication and operation processes. The electrochemical properties were investigated *via* cyclic voltammetry (CV) measurement and the HOMO/LUMO energy levels were obtained by calculating from the respective onset oxidation/reduction potentials. According to the onsets of the oxidation curves (relative to the ferrocene/ferrocenium reference) (Fig. 2b), the oxidation potentials of the six compounds were very close to each other and their corresponding HOMO energy levels were all around  $-5.30\text{ eV}$ . The reduction potentials were decreased significantly in *cis*-PyCNTPA, *trans*-PyCNTPA and *trans*-PyCNDPA and they all showed deeper LUMO levels of  $-3.60\text{ eV}$ , which were all about  $0.22\text{ eV}$  lower than respective *cis*-PyPTPA, *trans*-PyPTPA and *trans*-PyPDPA. The PQC�N unit could deepen the LUMO energy level and effectively contributed to the device performance because of the relatively facile transfer of electrons. These experimental data demonstrated the same trend as the theoretical results obtained from the DFT calculations. The CV measurements suggested lower HOMO–LUMO gaps of around  $2.15\text{ eV}$ – $2.84\text{ eV}$ , implying that red/NIR emission could be successfully achieved.

### Photophysical properties

For the purpose of exploring the photophysical properties of these compounds, the UV-vis absorption and photoluminescence characteristics were further tested. As shown in Fig. 3a, in dilute toluene solution, the absorption spectra of the six compounds showed similar absorption profiles with three main absorption bands. The intense high-energy absorption bands at around  $280\text{ nm}$  and  $330\text{ nm}$  were ascribed to the localized  $n\text{-}\pi^*$  and  $\pi\text{-}\pi^*$  transitions of the aromatic amines and rigid acceptors PQP and PQC�N. The structureless long-wavelength broad absorption bands in the range of  $410\text{--}546\text{ nm}$  originated from the ICT transition from the donor moieties (DPA/TPA) to the acceptor units (PQP/PQC�N). They displayed various ICT emissions and structureless PL spectra ranging from the orange-red to deep-red region in toluene solutions (Fig. 3b). As expected, *cis*-PyCNTPA,

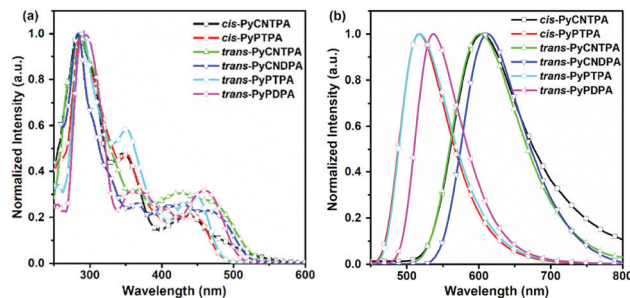


Fig. 3 (a) UV-vis absorption spectra in toluene solutions ( $10^{-5}\text{ M}$ ) and (b) normalized fluorescence spectra in toluene solutions ( $10^{-5}\text{ M}$ ) of *cis*-PyCNTPA, *cis*-PyPTPA, *trans*-PyCNTPA, *trans*-PyCNDPA, *trans*-PyPTPA and *trans*-PyPDPA.

*trans*-PyCNTPA and *trans*-PyCNDPA using CN groups as the co-acceptor showed significant red-shifts with emission maxima at  $607\text{ nm}$ ,  $602\text{ nm}$  and  $615\text{ nm}$  as compared with their counterparts of *cis*-PyPTPA ( $517\text{ nm}$ ), *trans*-PyPTPA ( $514\text{ nm}$ ) and *trans*-PyPDPA ( $536\text{ nm}$ ).

It can also be seen that the two pairs of *cis/trans*-isomers, *cis*-PyCNTPA/*trans*-PyCNTPA and *cis*-PyPTPA/*trans*-PyPTPA all displayed very identical emission spectra and emission peaks with only several nanometers' variations, suggesting that the molecular configuration had little effect on the emission color. By changing the polarity of the solvent (Fig. S9 and Table S2, ESI $^{\dagger}$ ), the maximum PL peak of *cis*-PyCNTPA showed a significant red shift from  $532\text{ nm}$  in nonpolar hexane to  $740\text{ nm}$  in polar chloroform. The *trans*-PyCNTPA and *trans*-PyCNDPA also showed the same trends with a red-shift from  $540\text{ nm}$  in hexane to  $722\text{ nm}$  in chloroform for *trans*-PyCNTPA, and  $554\text{ nm}$  in hexane to  $676\text{ nm}$  in chloroform for *trans*-PyCNDPA. This is the general feature for most of the organic D–A type molecules with substantial CT characters. The solvatochromic effects of *cis*-PyPTPA, *trans*-PyPTPA and *trans*-PyPDPA were not very obvious as their PL peaks showed less red-shifts than *cis*-PyCNTPA, *trans*-PyCNTPA and *trans*-PyCNDPA with increasing solvent polarity, suggesting the relatively weak electron-withdrawing ability of the PQP unit.

The effective process of cross-system crossing is the basic characteristic of TADF material, which requires the molecule to have enough small  $\Delta E_{\text{ST}}$ . The fluorescence and phosphorescence spectra of these compounds were, respectively, investigated in the dilute toluene at room temperature and at a low temperature ( $77\text{ K}$ ), and the experimental  $S_1$  and  $T_1$  energies were calculated from the onsets of the fluorescence and phosphorescence spectra (Fig. 4b and Fig. S10, ESI $^{\dagger}$ ). The experimental  $\Delta E_{\text{ST}}$  values were calculated to be  $0.10\text{ eV}$  for *cis*-PyCNTPA,  $0.11\text{ eV}$  for *trans*-PyCNTPA,  $0.08\text{ eV}$  for *trans*-PyCNDPA,  $0.34\text{ eV}$  for *cis*-PyPTPA,  $0.34\text{ eV}$  for *trans*-PyPTPA and  $0.29\text{ eV}$  for *trans*-PyPDPA. In all, the *cis*-PyCNTPA, *trans*-PyCNTPA and *trans*-PyCNDPA using PQC�N as acceptors all manifested much smaller  $\Delta E_{\text{ST}}$  to ensure the efficient RISC process from triplet excited state to singlet excited state. In order to explore the TADF behavior, the transient PL characteristics were also studied. The transient PL decay curves of *cis*-PyCNTPA, *trans*-PyCNTPA and *trans*-PyCNDPA in doped films

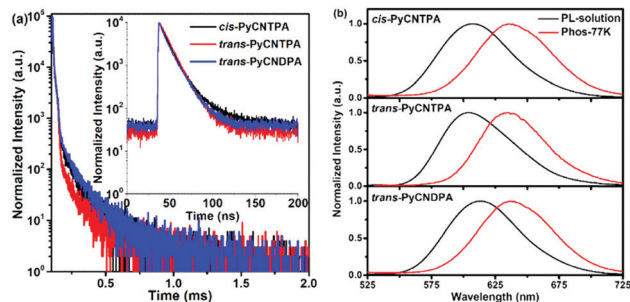


Fig. 4 (a) Transient PL curves of *cis*-PyCNTPA, *trans*-PyCNTPA and *trans*-PyCNDPA (1.0 wt%) doped into PMMA hosts (Inset: Prompt components). (b) Normalized fluorescence and phosphorescence (77 K) spectra of *cis*-PyCNTPA, *trans*-PyCNTPA and *trans*-PyCNDPA in toluene solutions ( $10^{-5}$  M).

all displayed biexponential decays with nanosecond order prompt fluorescence decays ( $\tau_F$ ) and microsecond order delayed fluorescence decays ( $\tau_{TADF}$ ) (Fig. 4a). However, the remaining compounds *cis*-PyPTPA, *trans*-PyPTPA and *trans*-PyDPDA only showed single exponential decays with the prompt  $\tau_F$ , illustrating that they were not emitters with delayed fluorescence (Fig. S11, ESI<sup>†</sup>). In the temperature-dependent transient PL spectra, with the temperature elevating from 100 to 300 K, the delayed component intensities of *cis*-PyCNTPA, *trans*-PyCNTPA and *trans*-PyCNDPA were all enhanced with the improving temperature, which were the typical TADF characteristics (Fig. 5 and Fig. S12, ESI<sup>†</sup>).

The fluorescence emission spectra of these compounds doped in the PMMA films were identical to their emissions in toluene solutions (Fig. S13, ESI<sup>†</sup>). By using an integrating

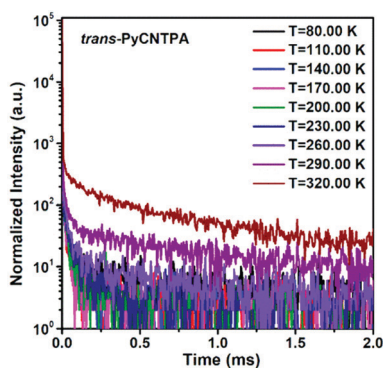


Fig. 5 Transient PL decay curve of the 1.0 wt% *trans*-PyCNTPA doped PMMA film at different temperatures.

sphere, the PLQYs of the six molecules in the doped films were also measured. The *trans*-isomers in the doped films exhibited a relatively high PLQY of 87% for *trans*-PyCNTPA, 83% for *trans*-PyCNDPA, 81% for *trans*-PyPTPA and 78% for *trans*-PyDPDA. While the *cis*-conformation molecules possessed lower PLQY of 19% for *cis*-PyCNTPA and 12% for *cis*-PyPTPA. This was in the same trend with the oscillator strengths as found in the theoretical calculations. The relevant radiative and nonradiative decay rate constants ( $k_r$  and  $k_{nr}$ ) were further calculated. In the excited state dynamics study, the  $k_r$  of *trans*-PyCNTPA was calculated to be  $4.10 \times 10^7 \text{ s}^{-1}$ , which was higher than that of *cis*-PyCNTPA ( $0.59 \times 10^7 \text{ s}^{-1}$ ). The  $k_{nr}$ s values of *trans*-PyCNTPA and *cis*-PyCNTPA were comparable. Similarly, *trans*-PyPTPA showed a  $k_r$  of  $19.96 \times 10^7 \text{ s}^{-1}$  which was also higher than that of *cis*-PyCNTPA ( $3.98 \times 10^7 \text{ s}^{-1}$ ). The  $k_{nr}$  of *trans*-PyPTPA was  $4.68 \times 10^7 \text{ s}^{-1}$  which was lower than that of *cis*-PyPTPA of  $29.18 \times 10^7 \text{ s}^{-1}$ . These results indicated that the molecular vibrational modes of excited state of *trans*-configuration could effectively hinder the energy loss *via* nonradiative decay paths and contributed to the higher efficiencies of the *trans*-isomers (Table 2).

### Electroluminescence properties

To explore the EL performance, the non-doped device was first fabricated with a normal sandwiched configuration of ITO/HAT-CN (6 nm)/TAPC (45 nm)/TCTA (5 nm)/Emitters (20 nm)/TmPyPb (40 nm)/LiF (1 nm)/Al (120 nm), in which ITO and Al served as the anode and cathode, HATCN (1,4,5,8,9,11-hexazatriphenylene-hexanitrile) was used as a hole injection layer, TAPC (di-(4-(*N,N*-ditolyl-amino)-phenyl)cyclohexane) and TCTA (4,4,4-tris(*N*-carbazolyl)triphenyl-amine) were applied as the hole transporting layer and exciton blocking layer, TmPyPb and LiF were used as the electron transporting layer and electron injecting layer, respectively. The devices exhibited electroluminescence in NIR regions with emission 712 nm for *trans*-PyCNDPA, respectively, corresponding to CIE coordinates of (0.65, 0.31), (0.67, 0.31) and (0.67, 0.30). The devices of the remaining three molecules of *cis*-PyPTPA, *trans*-PyPTPA and *trans*-PyDPDA also showed red emissions with the CIE coordinates of (0.51, 0.47), (0.42, 0.55) and (0.45, 0.54), respectively. Regrettably, the non-doped OLEDs all showed quite low EQEs due to the insufficient utilization of triplet excitons or triplet-triplet annihilations in these non-doped devices (Table S3, ESI<sup>†</sup>).

The multilayered OLEDs with different device configurations were further fabricated. OLEDs based on dopants were fabricated with a normal sandwiched configuration: ITO/HATCN (6 nm)/TAPC

Table 2 Photophysical properties of *cis*-PyCNTPA, *cis*-PyPTPA, *trans*-PyCNTPA, *trans*-PyCNDPA, *trans*-PyPTPA and *trans*-PyDPDA

Compound	$\Phi_{PL}^a$ (%)	$\Delta E_{St}$ (eV)	$k_r$ ( $10^7 \text{ s}^{-1}$ )	$k_{nr}$ ( $10^7 \text{ s}^{-1}$ )	$\tau_F$ (ns)	$\tau_{TADF}$ ( $\mu\text{s}$ )	$k_{IC}$ ( $10^7 \text{ s}^{-1}$ )	$k_{ISC}$ ( $10^7 \text{ s}^{-1}$ )	$k_{TADF}$ ( $10^4 \text{ s}^{-1}$ )
<i>cis</i> -PyCNTPA	19	0.10	0.59	0.25	10.30	24.36	2.52	6.60	7.80
<i>cis</i> -PyPTPA	12	0.34	3.98	29.18	3.02	—	—	—	—
<i>trans</i> -PyCNTPA	87	0.11	4.10	0.61	10.78	12.67	0.61	4.56	6.81
<i>trans</i> -PyPTPA	81	0.34	19.96	4.68	4.06	—	—	—	—
<i>trans</i> -PyCNDPA	83	0.08	2.84	0.58	9.44	26.02	0.58	7.17	3.19
<i>trans</i> -PyDPDA	78	0.29	21.05	5.94	3.71	—	—	—	—

<sup>a</sup>  $\Phi_{PL}$ : photoluminescence quantum yields of 1 wt% doped PMMA thin films.

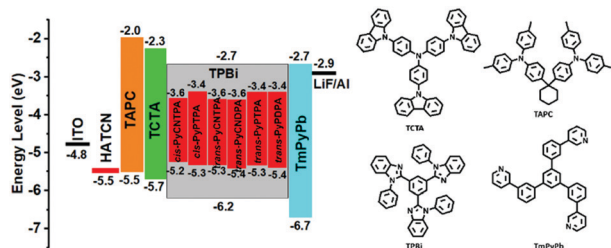


Fig. 6 The device structure and energy level diagram and molecular structures of the materials employed in the devices.

(45 nm)/TCTA (5 nm)/TPBi:emitter (20 nm)/TmPyPb (40 nm)/LiF (1 nm)/Al (120 nm). In the EML, these compounds were doped into the host 1,3,5-tris(1-phenyl-1H-benzimidazol-2-yl)benzene (TPBi) with 10 wt% concentration. The corresponding molecular structures, energy level diagrams and the architectures of the devices are depicted in Fig. 6.

The OLEDs based on *trans*-PyCNDPA, *cis*-PyCNTPA and *trans*-PyCNTPA exhibited deep-red emission with electroluminescent

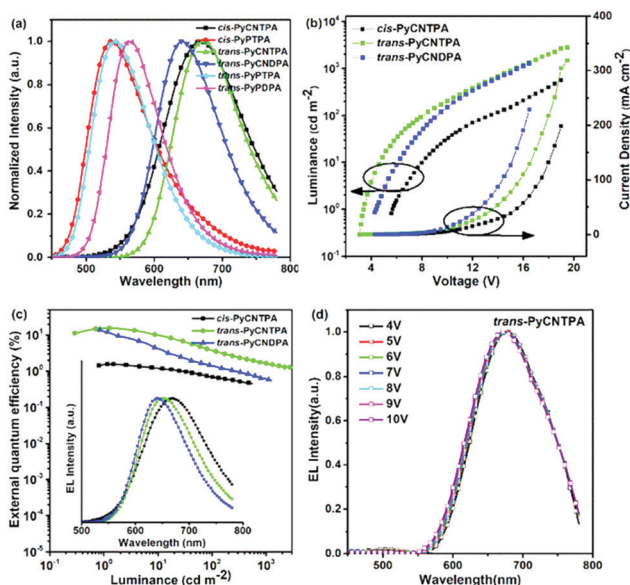


Fig. 7 (a) EL spectra of the devices at 100  $\text{cd m}^{-2}$ . (b) Luminance curves—voltage—current density curves of devices based on *cis*-PyCNTPA, *trans*-PyCNTPA and *trans*-PyCNDPA. (c) EQE—luminance and the EL spectra of OLEDs based on *cis*-PyCNTPA, *trans*-PyCNTPA and *trans*-PyCNDPA. (d) The EL spectra of *trans*-PyCNTPA measured at 4–10 V.

peaks at 640 nm, 669 nm and 668 nm, and Commission Internationale de L'Eclairage (CIE) coordinates of (0.64, 0.35), (0.63, 0.36) and (0.66, 0.35), respectively, meeting the basic requirements for deep-red emission ( $\lambda_{\text{max}} > 620 \text{ nm}$  and CIE coordinates of  $x \geq 0.60$ ,  $y \leq 0.40$ ). The EL spectra were all in good accordance with their PL emission spectra measured in doped films (Fig. 7a), illustrating that the electroluminescence originated from the pure emissive layers and energy transfers from the TPBi host to emitters absolutely occurred in the EL process.

The devices based on the compounds with PQQ as the acceptor showed poor performance with the maximum EQE of 0.40%, 5.12% and 6.42% for *cis*-PyPTPA, *trans*-PyPTPA and *trans*-PyPDPA, respectively. As the CN was introduced as the co-acceptor, the corresponding device performance of *cis*-PyCNTPA, *trans*-PyCNTPA and *trans*-PyCNDPA demonstrated significant improvement. As a result, the maximum EQE reached 15.5% with the deep-red emission of 668 nm for *trans*-PyCNTPA without any optical out-coupling optimization attributing to the effective utilization of the triplet excitons in OLEDs, which is a very descent result among the deep-red TADF OLEDs with an EL peak wavelength at 660 nm as compared to previously reported data. In comparison, the OLED based on *cis*-PyCNTPA showed a maximum EQE of only 1.56% which was due to its extremely low PLQY. In addition, the turn-on voltage of the OLED based on *trans*-PyCNTPA was significantly lower than that of *cis*-PyCNTPA. The *cis*-PyCNTPA exhibited significantly lower electroluminescence efficiency and photoluminescence efficiency, indicating that exciton utilization efficiency is lower than *trans*-PyCNTPA. The turn-on voltage refers to the driving voltage of the device at the brightness of  $1 \text{ cd m}^{-2}$ . Due to the low exciton utilization efficiency, higher turn-on voltage was needed to produce more excitons to achieve the brightness of  $1 \text{ cd m}^{-2}$ , which might result in higher turn-on voltage for the doped device based on *cis*-PyCNTPA. Therefore, the doped device based on *cis*-PyCNTPA exhibited much higher turn-on voltage compared with the doped device based on *trans*-PyCNTPA. EL characteristics of OLEDs based on these *cis*-PyCNTPA, *trans*-PyCNTPA, *trans*-PyCNDPA, *cis*-PyPTPA, *trans*-PyPTPA and *trans*-PyCNDPA are shown in Fig. 7b–c and Fig. S14a–c (ESI<sup>†</sup>), and the detailed data are summarized in Table 3.

All the devices showed stable spectra under different voltages (Fig. 7d and Fig. S15, ESI<sup>†</sup>). These results revealed that the fine modulation of molecular structure and rational *cis*-*trans*-isomeric strategy is an effective method to explore the structure–property

Table 3 The EL performances of doped devices based on *cis*-PyCNTPA, *cis*-PyPTPA, *trans*-PyCNTPA, *trans*-PyCNDPA, *trans*-PyPTPA and *trans*-PyPDPA

Device	$V_{\text{on}}^a$ (V)	$L_{\text{max}}^b$ ( $\text{cd m}^{-2}$ )	$\text{CE}_{\text{max}}^c$ ( $\text{cd A}^{-1}$ )	$\text{PE}_{\text{max}}^d$ ( $\text{lm W}^{-1}$ )	EQE <sup>e</sup> (%) max/100 $\text{cd m}^{-2}$	EL $\lambda_{\text{max}}^f$ (nm)	CIE <sup>g</sup> (x,y)
<i>cis</i> -PyCNTPA	5.9	555	0.95	0.51	1.56/0.70	669	(0.63,0.36)
<i>cis</i> -PyPTPA	4.5	469	1.19	0.83	0.40/0.22	536	(0.39,0.56)
<i>trans</i> -PyCNTPA	3.5	2769	10.5	9.46	15.50/3.50	668	(0.66,0.35)
<i>trans</i> -PyCNDPA	4.3	1258	11.2	8.21	13.90/1.31	640	(0.64,0.35)
<i>trans</i> -PyPTPA	3.8	4495	16.9	13.95	5.12/1.87	544	(0.39,0.56)
<i>trans</i> -PyPDPA	3.8	2871	20.3	16.77	6.42/1.54	560	(0.45,0.54)

<sup>a</sup>  $V_{\text{on}}$ : turn-on voltage at the luminescence of  $1 \text{ cd m}^{-2}$ . <sup>b</sup>  $L_{\text{max}}$ : maximum luminance. <sup>c</sup>  $\text{CE}_{\text{max}}$ : maximum current efficiency. <sup>d</sup>  $\text{PE}_{\text{max}}$ : maximum power efficiency. <sup>e</sup> EQE: external quantum efficiency of maximum/at  $100 \text{ cd m}^{-2}$ . <sup>f</sup> EL  $\lambda_{\text{max}}$ : EL emission peak of EL spectrum at  $100 \text{ cd m}^{-2}$ . <sup>g</sup> CIE: commission International de l'Eclairage (CIE) coordinates at  $100 \text{ cd m}^{-2}$ .

relationship and obtain high-efficiency deep-red materials and OLEDs.

## Conclusions

In summary, two pairs of isomers of *trans*-PyCNTPA/*cis*-PyCNTPA and *trans*-PyPTPA/*cis*-PyPTPA adopting the same TPA donor and two different kinds of electron acceptors (PQP and PQCN) with different donor connecting strategies were designed and synthesized. Two model compounds *trans*-PyCNDPA and *trans*-PyPDPA using DPA as the donor were also obtained. By manipulating the substitution position of the donor and electron-withdrawing strength of the acceptor, the emission colors are facily shifted from the orange-red (*trans*-PyPTPA/*cis*-PyPTPA/*trans*-PyPDPA) to deep-red region (*trans*-PyCNTPA/*cis*-PyCNTPA/*trans*-PyCNDPA). The co-acceptor CN unit is crucial to obtain TADF features. The *cis*-PyCNTPA, *trans*-PyCNTPA and *trans*-PyCNDPA all manifested smaller  $\Delta E_{ST}$  than *cis*-PyPTPA, *trans*-PyPTPA and *trans*-PyPDPA to ensure the efficient RISC process from the triplet excited state to the singlet excited state. The experimental data and theoretical calculations all indicate enhanced  $\Phi_{PL,S}$  values in *trans*-isomers, that is, 87% for *trans*-PyCNTPA, 83% for *trans*-PyCNDPA, 81% for *trans*-PyPTPA and 78% for *trans*-PyPDPA, which are remarkably higher than those of *cis*-PyCNTPA (19%) and *cis*-PyPTPA (12%). The *trans*-configuration can effectively hinder the energy loss via nonradiative decay paths and result in higher efficiency. The TADF-OLED based on *trans*-PyCNTPA realizes the state-of-the-art device performance with a high EQE of 15.5% and the electroluminescent peak of 668 nm in the deep-red region. These findings would provide meaningful instructions to achieve highly efficient red TADF emitters by isomeric modulation for OLED investigation and applications.

## Conflicts of interest

There are no conflicts to declare.

## Acknowledgements

This research is supported by the National Natural Science Foundation of China (91833304, 21774047, and 22075100), the Open Fund of the State Key Laboratory of Luminescent Materials and Devices (South China University of Technology, 2021-skllmd) and the Fundamental Research Funds for the Central Universities.

## Notes and references

- D. Wu, L. Chen, W. Lee, G. Ko, J. Yin and J. Yoon, *Coord. Chem. Rev.*, 2018, **354**, 74–97.
- L. Yuan, W. Lin, K. Zheng, L. He and W. Huang, *Chem. Soc. Rev.*, 2013, **42**, 622–661.
- S. Qi, S. Kim, V. N. Nguyen, Y. Kim, G. Niu, G. Kim, S. J. Kim, S. Park and J. Yoon, *ACS Appl. Mater. Interfaces*, 2020, **12**, 51293–51301.
- H. Zhou, X. Zeng, A. Li, W. Zhou, L. Tang, W. Hu, Q. Fan, X. Meng, H. Deng, L. Duan, Y. Li, Z. Deng, X. Hong and Y. Xiao, *Nat. Commun.*, 2020, **11**, 6183.
- S. Zhu, Z. Hu, R. Tian, B. C. Yung, Q. Yang, S. Zhao, D. O. Kiesewetter, G. Niu, H. Sun, A. L. Antaris and X. Chen, *Adv. Mater.*, 2018, **30**, 1802546.
- F. Ni, N. Li, L. Zhan and C. Yang, *Adv. Opt. Mater.*, 2020, **8**, 1902187.
- N. R. Paisley, C. M. Tonge and Z. M. Hudson, *Front. Chem.*, 2020, **8**, 229.
- D. Wang, M. M. S. Lee, G. Shan, R. T. K. Kwok, J. W. Y. Lam, H. Su, Y. Cai and B. Z. Tang, *Adv. Mater.*, 2018, **30**, 1802105.
- S. Koyama, Y. Inaba, M. Kasano and T. Murata, *IEEE Trans. Electron Devices*, 2008, **55**, 754–759.
- B. Stender, S. F. Volker, C. Lambert and J. Pflaum, *Adv. Mater.*, 2013, **25**, 2943–2947.
- D.-H. Kim, A. D'Aléo, X.-K. Chen, A. D. S. Sandanayaka, D. Yao, L. Zhao, T. Komino, E. Zaborova, G. Canard, Y. Tsuchiya, E. Choi, J. W. Wu, F. Fages, J.-L. Brédas, J.-C. Ribierre and C. Adachi, *Nat. Photonics*, 2018, **12**, 98–104.
- H. Chen, L. Sun, G.-D. Li and X. Zou, *Chem. Mater.*, 2018, **30**, 2018–2027.
- H. U. Kim, S. Sohn, W. Choi, M. Kim, S. U. Ryu, T. Park, S. Jung and K. S. Bejoymohandas, *J. Mater. Chem. C*, 2018, **6**, 10640–10658.
- J. X. Chen, W. W. Tao, W. C. Chen, Y. F. Xiao, K. Wang, C. Cao, J. Yu, S. Li, F. X. Geng, C. Adachi, C. S. Lee and X. H. Zhang, *Angew. Chem., Int. Ed.*, 2019, **58**, 14660–14665.
- W. Zeng, H. Y. Lai, W. K. Lee, M. Jiao, Y. J. Shiu, C. Zhong, S. Gong, T. Zhou, G. Xie, M. Sarma, K. T. Wong, C. C. Wu and C. Yang, *Adv. Mater.*, 2018, **30**, 1704961.
- U. Balijapalli, R. Nagata, N. Yamada, H. Nakanotani, M. Tanaka, A. D'Aleo, V. Placide, M. Mamada, Y. Tsuchiya and C. Adachi, *Angew. Chem., Int. Ed.*, 2021, **60**, 8477–8482.
- Y. L. Zhang, Q. Ran, Q. Wang, Y. Liu, C. Hanisch, S. Reineke, J. Fan and L. S. Liao, *Adv. Mater.*, 2019, **31**, 1902368.
- J. H. Kim, J. H. Yun and J. Y. Lee, *Adv. Opt. Mater.*, 2018, **6**, 1800255.
- F.-M. Xie, X.-Y. Zeng, J.-X. Zhou, Z.-D. An, W. Wang, Y.-Q. Li, X.-H. Zhang and J.-X. Tang, *J. Mater. Chem. C*, 2020, **8**, 15728–15734.
- K. Sun, D. Liu, W. Tian, F. Gu, W. Wang, Z. Cai, W. Jiang and Y. Sun, *J. Mater. Chem. C*, 2020, **8**, 11850–11859.
- S. Kothavale, W. J. Chung and J. Y. Lee, *J. Mater. Chem. C*, 2021, **9**, 528–536.
- J. Jin, W. Wang, P. Xue, Q. Yang, H. Jiang, Y. Tao, C. Zheng, G. Xie, W. Huang and R. Chen, *J. Mater. Chem. C*, 2021, **9**, 2291–2297.
- X. Gong, P. Li, Y. H. Huang, C. Y. Wang, C. H. Lu, W. K. Lee, C. Zhong, Z. Chen, W. Ning, C. C. Wu, S. Gong and C. Yang, *Adv. Funct. Mater.*, 2020, **30**, 1908839.
- J. Jiang, X. Li, M. Hanif, J. Zhou, D. Hu, S. Su, Z. Xie, Y. Gao, B. Yang and Y. Ma, *J. Mater. Chem. C*, 2017, **5**, 11053–11058.
- H. Kaji, H. Suzuki, T. Fukushima, K. Shizu, K. Suzuki, S. Kubo, T. Komino, H. Oiwa, F. Suzuki, A. Wakamiya, Y. Murata and C. Adachi, *Nat. Commun.*, 2015, **6**, 8476.

- 26 Y. Xu, X. Liang, X. Zhou, P. Yuan, J. Zhou, C. Wang, B. Li, D. Hu, X. Qiao, X. Jiang, L. Liu, S. J. Su, D. Ma and Y. Ma, *Adv. Mater.*, 2019, **31**, 1807388.
- 27 M. Li, Y.-F. Wang, D.-W. Zhang, D. Zhang, Z.-Q. Hu, L. Duan and C.-F. Chen, *Sci. China: Mater.*, 2021, **64**, 899–908.
- 28 Y. Zhang, D. Zhang, J. Wei, Z. Liu, Y. Lu and L. Duan, *Angew. Chem., Int. Ed.*, 2019, **58**, 16912–16917.
- 29 L. Yu, Z. Wu, G. Xie, W. Zeng, D. Ma and C. Yang, *Chem. Sci.*, 2018, **9**, 1385–1391.
- 30 Z. Chen, F. Ni, Z. Wu, Y. Hou, C. Zhong, M. Huang, G. Xie, D. Ma and C. Yang, *J. Phys. Chem. Lett.*, 2019, **10**, 2669–2675.
- 31 C. Adachi, M. A. Baldo, M. E. Thompson and S. R. Forrest, *J. Appl. Phys.*, 2001, **90**, 5048–5051.
- 32 C. W. Tang and S. A. VanSlyke, *Appl. Phys. Lett.*, 1987, **51**, 913–915.
- 33 S. Ohisa, T. Takahashi, M. Igarashi, H. Fukuda, T. Hikichi, R. Komatsu, E. Ueki, Y. J. Pu, T. Chiba and J. Kido, *Adv. Funct. Mater.*, 2019, **29**, 1808022.
- 34 L. S. Cui, H. Nomura, Y. Geng, J. U. Kim, H. Nakanotani and C. Adachi, *Angew. Chem., Int. Ed.*, 2017, **56**, 1571–1575.
- 35 F. Liu, X. Man, H. Liu, J. Min, S. Zhao, W. Min, L. Gao, H. Jin and P. Lu, *J. Mater. Chem. C*, 2019, **7**, 14881–14888.
- 36 D. Przemyslaw, P. P. Masato, O. T. Youhei, M. Satoshi and P. M. Andrew, *Angew. Chem., Int. Ed.*, 2016, **55**, 5739–5744.
- 37 C. Li, R. Duan, B. Liang, G. Han, S. Wang, K. Ye, Y. Liu, Y. Yi and Y. Wang, *Angew. Chem., Int. Ed.*, 2017, **56**, 11525–11529.
- 38 Y. Tao, K. Yuan, T. Chen, P. Xu, H. Li, R. Chen, C. Zheng, L. Zhang and W. Huang, *Adv. Mater.*, 2014, **26**, 7931–7958.
- 39 Y. Im, M. Kim, Y. J. Cho, J.-A. Seo, K. S. Yook and J. Y. Lee, *Chem. Mater.*, 2017, **29**, 1946–1963.
- 40 B. Zhao, H. Wang, C. Han, P. Ma, Z. Li, P. Chang and H. Xu, *Angew. Chem., Int. Ed.*, 2020, **59**, 19042–19047.
- 41 T. Wang, K. Li, B. Yao, Y. Chen, H. Zhan, Z. Xie, G. Xie, X. Yi and Y. Cheng, *Adv. Funct. Mater.*, 2020, **30**, 2002493.
- 42 W. Li, Z. Li, C. Si, M. Y. Wong, K. Jinnai, A. K. Gupta, R. Kabe, C. Adachi, W. Huang, E. Zysman-Colman and I. D. W. Samuel, *Adv. Mater.*, 2020, **32**, 2003911.
- 43 D. G. Congrave, B. H. Drummond, P. J. Conaghan, H. Francis, S. T. E. Jones, C. P. Grey, N. C. Greenham, D. Credgington and H. Bronstein, *J. Am. Chem. Soc.*, 2019, **141**, 18390–18394.
- 44 X. Gong, C.-H. Lu, W.-K. Lee, P. Li, Y.-H. Huang, Z. Chen, L. Zhan, C.-C. Wu, S. Gong and C. Yang, *Chem. Eng. J.*, 2021, **405**, 126663.
- 45 J. Xue, Q. Liang, R. Wang, J. Hou, W. Li, Q. Peng, Z. Shuai and J. Qiao, *Adv. Mater.*, 2019, **31**, 1808242.
- 46 H. Liu, J. Li, W.-C. Chen, Z. Chen, Z. Liu, Q. Zhan, X. Cao, C.-S. Lee and C. Yang, *Chem. Eng. J.*, 2020, **401**, 126107.
- 47 Z. Qiu, W. Xie, Z. Yang, J.-H. Tan, Z. Yuan, L. Xing, S. Ji, W.-C. Chen, Y. Huo and S.-J. Su, *Chem. Eng. J.*, 2021, **415**, 128949.
- 48 M. M. Islam, Z. Hu, Q. Wang, C. Redshaw and X. Feng, *Mater. Chem. Front.*, 2019, **3**, 762–781.
- 49 J. Y. Hu, Y. J. Pu, G. Nakata, S. Kawata, H. Sasabe and J. Kido, *Chem. Commun.*, 2012, **48**, 8434–8436.
- 50 C.-J. Ou, B.-Y. Ren, J.-W. Li, D.-Q. Lin, C. Zhong, L.-H. Xie, J.-F. Zhao, B.-X. Mi, H.-T. Cao and W. Huang, *Org. Electron.*, 2017, **43**, 87–95.
- 51 T. Yang, Z. Cheng, Z. Li, J. Liang, Y. Xu, C. Li and Y. Wang, *Adv. Funct. Mater.*, 2020, **30**, 2002681.
- 52 H. Liu, L. Kang, J. Li, F. Liu, X. He, S. Ren, X. Tang, C. Lv and P. Lu, *J. Mater. Chem. C*, 2019, **7**, 10273–10280.
- 53 Y. Liu, H. Liu, Q. Bai, C. Du, A. Shang, D. Jiang, X. Tang and P. Lu, *ACS Appl. Mater. Interfaces*, 2020, **12**, 16715–16725.
- 54 K.-C. Pan, S.-W. Li, Y.-Y. Ho, Y.-J. Shiu, W.-L. Tsai, M. Jiao, W.-K. Lee, C.-C. Wu, C.-L. Chung, T. Chatterjee, Y.-S. Li, K.-T. Wong, H.-C. Hu, C.-C. Chen and M.-T. Lee, *Adv. Funct. Mater.*, 2016, **26**, 7560–7571.
- 55 F. Xie, H. Ran, X. Duan, R. Han, H. Sun and J.-Y. Hu, *J. Mater. Chem. C*, 2020, **8**, 17450–17456.
- 56 B.-B. Ma, Y.-X. Peng, P.-C. Zhao and W. Huang, *Tetrahedron*, 2015, **71**, 3195–3202.
- 57 Y. Liu, T. Shan, L. Yao, Q. Bai, Y. Guo, J. Li, X. Han, W. Li, Z. Wang, B. Yang, P. Lu and Y. Ma, *Org. Lett.*, 2015, **17**, 6138–6141.